Properties of light stratiform rain derived from 10- and 94-GHz airborne Doppler radars measurements

Lin Tian,[1,2] Gerald M. Heymsfield,[2] Lihua Li,[1,2] and Ramesh C. Srivastava[3]

Received 12 October 2006; revised 12 January 2007; accepted 16 February 2007; published 12 June 2007.

[1] This paper presents an initial investigation of using airborne Doppler radar operating at 10 and 94 GHz to measure the light stratiform rain ($\leq$5 mm hr^{-1}). It has been shown that the combination of 10 and 94 GHz is more sensitive to resolve the raindrop size distribution (RSD) in light rain than that of 14 and 35 GHz. A case of light stratiform rain over southern Florida is examined in detail in this study. Techniques for retrieving the profiles of a Gamma raindrop size distribution (RSD), vertical air velocity, and attenuation by precipitation and water vapor are presented. This approach uses the difference of the Doppler velocity at two frequencies and yields both RSD and the vertical air motion. The approach is primarily applicable to rain rates less than 5 mm hr^{-1}. The magnitudes of the retrieved RSD are similar to those found in ground-based observations of light stratiform rain. The retrieved vertical winds with downdrafts below about 3 km and weak updraft above are similar to what has been observed in widespread stratiform rain with melting band. The sensitivities of the retrieval to Gamma shape parameter are discussed.

Citation: Tian, L., G. M. Heymsfield, L. Li, and R. C. Srivastava (2007), Properties of light stratiform rain derived from 10- and 94-GHz airborne Doppler radars measurements, *J. Geophys. Res.*, *112*, D11211, doi:10.1029/2006JD008144.

1. Introduction

[2] The vertical profiles of raindrop size distribution (RSD), vertical air velocity, precipitation, and water vapor distribution are important for studying the latent heating/cooling profile of precipitation yet are difficult to measure. Over the past several years, the Tropical Rainfall Measuring Mission (TRMM) [*Kummerow et al.*, 2000] has provided data for improving weather prediction and understanding precipitation structure and formation. Measurements by the single-wavelength TRMM precipitation radar (PR) have been used to estimate attenuation-corrected reflectivity and, from that, the rainfall rate [*Iguchi et al.*, 2000]. The data have also been used in conjunction with numerical cloud models to estimate latent heating/cooling [*Tao et al.*, 2000].

[3] One of the main uncertainties in estimating rainfall rate from the TRMM single-wavelength PR is the variability in the raindrop size distribution (RSD). A dual-wavelength radar, with a carefully selected frequency pair, can help to reduce this uncertainty. The upcoming Global Precipitation Measurement (GPM) dual-frequency radar (14 and 35 GHz) can provide RSD information and hence improve the accuracy of rainfall estimation. Many dual-frequency rain-profiling algorithms have been proposed to date, starting with those developed by *Eccles and Muller* [1971], *Fujita* [1983], *Meneghini et al.* [1992], and *Marzoug and Amayenc* [1994]. These approaches start by assuming a two-parameter analytic RSD and proceed to develop a procedure to retrieve the parameters given the reflectivity profiles at the two frequencies. Doppler velocities are not considered in those approaches. At vertical incidence, the Doppler velocity is essentially due to the vertical air velocity and the fall velocity of the scattering particles. A number of investigators have shown that, under certain assumptions, the vertical air velocity and raindrop size distribution can be deduced from the mean Doppler velocity and reflectivity [e.g., *Atlas and Matejka*, 1985; *Ulbrich*, 1991]. Basic limitations of these methods are the errors incurred because of errors in deduced vertical winds and the effect of the turbulence. *Meneghini et al.* [2003] has explored the possibility of using the difference of Doppler velocities at 13.6 and 35 GHz, which is not affected by the vertical air motion, to improve the RSD estimation.

[4] In this study, we use a dual-frequency Doppler radar system operating at 10 and 94 GHz. In light rain, this system may resolve the RSD better than the GPM frequency pair because the difference in reflectivities at 14 and 35 GHz is small [*Haddad et al.*, 2006] compared to that at 10 and 94 GHz. Moreover, Doppler velocities measured by our system help to further resolve the RSD at vertical incidence. A disadvantage of the 94-GHz frequency is that it suffers greater attenuation than the GPM frequencies. This limits the 94 GHz system to light rain of intensity $\leq$5 mm hr^{-1}, but it would be capable of detecting much lighter rain (and high level ice clouds) than either the GPM or the TRMM radars. Moreover, light rain may have a greater impact on

[1]Goddard Earth Science and Technology Center, University of Maryland, Baltimore County, Maryland, USA.
[2]NASA Goddard Space Flight Center, Greenbelt, Maryland, USA.
[3]Department of the Geophysical Sciences, The University of Chicago, Chicago, Illinois, USA.

0148-0227/07/2006JD008144

the global energy balance because of its greater temporal and area extent. For example, using TRMM overpasses, *Schumacher and Houze* [2003] showed that 46% of rain area falls below 18 dBZ and accounts for 2.3% of rainfall.

[5] The main objective of this work is to provide an initial evaluation of the potential utility of combining 10- and 94-GHz Doppler radar measurements of light rain. Using two nadir-looking airborne Doppler radars, the ER-2 Doppler Radar (EDOP), and Cloud Radar System (CRS), mounted on NASA's ER-2 high-altitude aircraft, a unique data set has been collected from stratiform rain in southern Florida during the Cirrus Regional Study of Tropical Anvils and Cirrus Layers—Florida Area Cirrus Experiment (CRYSTAL-FACE) campaign in July 2002. The EDOP is a 10-GHz Doppler radar that has been used for several TRMM and other field experiments for observations of hurricanes [*Heymsfield et al.*, 1996]. The CRS [*Li et al.*, 2004] is a 94-GHz pulsed polarimetric Doppler radar and provides measurements similar to those of the CloudSat [*Stephens et al.*, 2002] cloud-profiling radar except that CloudSat does not have Doppler capability. These aircraft observations provide a unique opportunity to assess the usefulness of the 10–94-GHz Doppler radar system for light rain measurements.

[6] In section 2, we summarize the basic equations for the dual-wavelength radar system. In section 3, we present our technique for retrieving the RSD parameters, the vertical air velocity, and the water vapor and melting band attenuations. A data description is presented in section 4. Results of application of the method to the observations are presented in section 5. We conclude with a summary and discussion in section 6.

2. Basic Equations

[7] This Section gives brief definitions of radar parameters to be used. The apparent radar reflectivity factor at millimeter wavelength at range r, $Z_{\rm mm}$ (r), is given by

$$Z_{\rm mm}(r) = Z^{(t)}_{\rm mm}(r) \times A_{\rm mm}(0,r). \tag{1}$$

Here $Z^{(t)}_{\rm mm}$ (r) represents the 'true' reflectivity at range r and $A_{\rm mm}(0, r)$ (≤ 1) is the two-way attenuation factor between the radar at $r = 0$ and the range r. The observed reflectivity will be denoted by $Z^{(\rm m)}_{mm}$ (r). It differs from $Z_{\rm mm}$ (r) because of measurement errors and, more fundamentally, because of insufficient averaging of the received power. The subscripts mm and cm will be used to denote the two wavelengths, 3.2 mm and 3.2 cm (94 and 10 GHz), respectively. The 'true' reflectivity is related to the target characteristics by

$$Z^{(t)}_{\rm mm} = c_z \int_{D_{\rm min}}^{D_{\rm max}} N(D)\sigma_{\rm BACK,mm}(D){\rm d}D\left({\rm mm}^6{\rm m}^{-3}\right) \tag{2}$$

where $N(D)({\rm cm}^{-4})$ is the concentration of drops of diameter D(cm) per unit diameter interval, $c_z = \dfrac{10^{12}\lambda^4}{\pi^5|K|^2}$ (cm^4), λ (cm) is the wavelength of the radar, $|K|^2$ is related to the refractive index of water, and $\sigma_{\rm BACK}(D)$ (cm^2) is the backscattering cross section of drop of diameter D. The integral is taken from a minimum diameter $D_{\rm min}$ to a maximum diameter $D_{\rm max}$. Similar equations hold for the centimeter wavelength. Usually, the reflectivity is expressed in logarithmic (dBZ) units. For the millimeter wavelength, equation (1) may be written as

$$\xi_{\rm mm}(r) = \xi^{(t)}_{\rm mm}(r) - \alpha_{\rm mm}(0,r), \tag{3}$$

where

$$\xi_{\rm mm} = 10\log_{10}(Z_{\rm mm}), \xi^{(t)}_{\rm mm} = 10\log_{10}\left(Z^{(t)}_{\rm mm}\right), \tag{4}$$

and

$$\alpha_{\rm mm}(0,r) = -10\log_{10}[A_{\rm mm}(0,r)], \tag{5}$$

is the two-way attenuation in dB between the radar and the range r. We decompose the attenuation into components of precipitation $\alpha^{\rm ppt}_{\rm mm}$ and atmospheric gases $\alpha^{\rm gas}_{\rm mm}$

$$\alpha_{\rm mm}(0,r) = \alpha^{\rm (gas)}_{\rm mm}(0,r) + \alpha^{\rm (ppt)}_{\rm mm}(0,r). \tag{6}$$

[8] At the millimeter wavelength considered here, water vapor is responsible for most of the gaseous attenuation. Attenuation by cloud water is ignored in this study. Above and in the melting layer, supercooled cloud water is present but it will not affect the retrieval below the melting layer. Below the melting layer, cloud water is not expected in the rain region of widespread stratiform rain with a melting band. This is because of the frequent occurrence of downdrafts in the rain region and rapid depletion of cloud water by the capture by raindrops. The one-way specific attenuation coefficient for rain is related to the target characteristics by

$$k = c_k \int_{D_{\rm min}}^{D_{\rm max}} N(D)\sigma_{\rm EXT}(D){\rm d}D. \tag{7}$$

Here k is in dB km^{-1}, $\sigma_{\rm EXT}$ (D) is the extinction cross section (cm^2) of drop of diameter D, and $c_k = 4.343 \times 10^5$.

[9] At vertical incidence, the mean Doppler velocity is given by

$$\bar{V}_{\rm cm} = \bar{V}^0_{\rm cm} - w, \tag{8}$$

where w is the vertical air velocity and $\bar{V}^0_{cm}$ is the mean Doppler velocity in the absence of vertical air motion; the latter is related to the target characteristics by

$$\bar{V}^0_{\rm cm} = \int_{D_{\rm min}}^{D_{\rm max}} N(D)\sigma_{\rm BACK,cm}(D)V_t(D){\rm d}D \Big/ \int_{D_{\rm min}}^{D_{\rm max}} N(D)\sigma_{\rm BACK,cm}(D){\rm d}D. \tag{9}$$

Here $V_t(D)$ is the terminal fall speed of drop of diameter D. The vertical air velocity is taken positive upwards, while the

mean Doppler velocity and the terminal fall speed are taken positive downward.

[10] The rainfall rate R is defined as

$$R = \frac{1}{6}\int_{D_{\min}}^{D_{\max}} N(D)D^3 V_t(D)\mathrm{d}D \tag{10}$$

3. Description of the Retrieval Procedures

[11] In this Section, we present the procedure for retrieving raindrop size distribution (RSD), vertical air velocity, and attenuation. We assume RSD to be a Gamma distribution [*Ulbrich*, 1983],

$$N(D) = N_0 D^{\mu}\exp(-\Lambda D). \tag{11}$$

Here $N(D)$ is the concentration of drops of diameter D per unit diameter interval. The distribution [equation (11)] is specified by the three parameters N_0, μ, and Λ. The slope Λ is related to the median volume diameter D_0 by $D_0 = (\mu + 3.67) / \Lambda$ if the distribution extends from zero to infinite diameters. Special forms of equation (11) are the exponential distribution ($\mu = 0$) and the Marshall-Palmer (M-P) distribution ($\mu = 0$, $N_0 = 8 \times 10^{-2}$ cm^{-4}) [*Marshall and Palmer*, 1948].

[12] Our observations provide four radar parameters, namely, two Doppler velocities and two reflectivites at the two wavelengths. From these observations, we can retrieve only two of the three parameters of RSD [equation (11)] in addition to vertical air velocity and the attenuation. Therefore we make the simplest assumption about the shape parameter μ, namely, that it has a constant value throughout the rain field. We then express N_0, D_o, and other parameters as function of the μ. In the following, we first show how to retrieve the parameters as a function of μ. Later on we will show that for light stratiform rain with melting band, the Doppler velocity measurements can be used to constrain the possible values of μ to a fairly narrow interval.

3.1. Retrieval of D_0 and w

[13] The differential mean Doppler velocity:

$$\Delta\bar{V} = \bar{V}_{\mathrm{cm}} - \bar{V}_{\mathrm{mm}} = \bar{V}^0_{\mathrm{cm}} - \bar{V}^0_{\mathrm{mm}} \tag{12}$$

is a function only of μ and D_0, independent of N_0, and vertical air velocity w. As we mentioned before, one of the uncertainties of using the Doppler velocity at a single wavelength to derive RSD is the uncertainty due to the vertical air motion. With the difference of the Doppler velocity at the two wavelengths, the vertical motions are cancelled out. We can write D_0 as a function of μ and $\Delta\bar{V}$,

$$D_0 = f_v(\mu, \Delta\bar{V}). \tag{13}$$

We obtain the function f_V as follows. We first calculate the backscattering cross sections of horizontally oriented ellipsoidal drops of the shape given by *Pruppacher and Pitter* [1971] using T-Matrix methods for nadir viewing [*Mishchenko et al.*, 2003]. Since the refractive index of water depends on the temperature, calculations were done for 5°, 15°, and 25°C, covering the range of temperatures in our observations. For the terminal fall speed, we use $V_t(D) = 9.65 - 10.30\exp(-6D)$(m s^{-1}) [*Atlas et al.*, 1973] for an air density ρ_0 near the ground. Doppler velocities observed aloft at a height having air density ρ were reduced to ground level by multiplying them by $(\rho / \rho_0)^{0.4}$ [*Foote and du Toit*, 1969]. The $D_{\min}$ and $D_{\max}$ were taken as 0.01 and 0.70 cm, respectively.

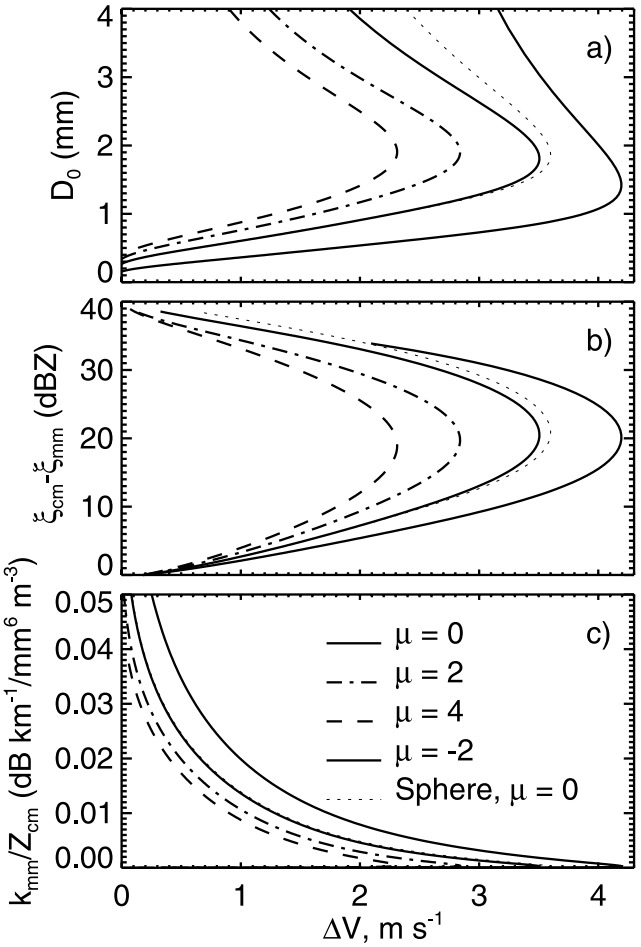

Figure 1. (a) Median drop size D_0 versus the difference of Doppler velocity at two wavelengths, $\Delta\bar{V} = \bar{V}_{\mathrm{cm}} - \bar{V}_{\mathrm{mm}}$; (b) difference of the reflectivity at the two wavelength, $\xi_{\mathrm{cm}} - \xi_{\mathrm{mm}}$ versus $\Delta\bar{V}$; (c) the ratio of the specific attenuation at millimeter wavelength (k_{mm}) and the reflectivity at centimeter wavelength (Z_{cm}) versus $\Delta\bar{V}$ for $\mu = -2$, 0, 2, 4 and ellipsoid. The results for spherical drop is plotted for $\mu = 0$.

[14] Figure 1a shows D_0 versus $\Delta\bar{V}$ for $\mu = -2$, 0, 2, 4, for the Pruppacher-Pitter drop shape and a temperature of 15°C. We have tested the sensitivity of the results to the drop-shape formulation using the drop shape given by *Andsager et al.* [1999]. The results are not shown because the difference between the two drop-shape formulations is less than 0.2%. The dotted curve in Figure 1a shows results for spherical drops for $\mu = 0$. The departures from spherical shape become noticeable at $D_0 \approx 1.5$ mm. Therefore it is important to consider the nonsphericity of the drops for $D_0 \geq 1.5$ mm.

[15] The differential Doppler velocity is small for small D_0, increases rapidly with increasing D_0, attains a maximum and then decreases with increasing D_0. Note that the maximum $\Delta\bar{V}$ decreases with increasing μ. It is about 3.5 m s^{-1} for $\mu = 0$ and 2.3 m s^{-1} for $\mu = 4$. The occurrence of a maximum in $\Delta\bar{V}$ can be used to constrain the possible values of μ. For example, if observed $\Delta\bar{V} > 2.3$ m s^{-1} then no solution for D_0 exists for $\mu > 4$.

[16] One potential complication in using Figure 1a to retrieve D_0 is that D_0 is a double-valued function of $\Delta\bar{V}$. However, it is not a problem in the case of stratiform rain. For example, for $\mu = 0$, the peak of the $\Delta\bar{V}$ which occurs at about $D_0 \cong 1.8$ mm ($\Lambda = 20$ cm^{-1}) corresponds to a rainfall rate of about 30 mm hr^{-1} [*Marshall and Palmer*, 1948]. In widespread stratiform rain, rainfall rates exceeding 10 mm hr^{-1} are unlikely. Therefore we can assume D_0 to be smaller than 1.8 mm and estimate it uniquely from $\Delta\bar{V}$. Moreover, we can usually reject one of the D_0 solutions based on the deduced vertical air velocity, for example, for $\Delta\bar{V}$ = 2.5 m s^{-1} Figure 1 gives $D_0 = 1$ or 3.2 mm for $\mu = 0$. For these D_0 values, we have $\bar{V}_{\rm cm}^{(0)} = 5.5$ or 8.5 m s^{-1}. The vertical air velocities implied by these two values of D_0 will differ by 3 m s^{-1}. Since in stratiform rain $|w|$ is generally less than 0.5 m s^{-1} [*Houze*, 1993], we should be able to reject one of the two D_0 solutions. Once D_0 has been estimated, we can calculate $\bar{V}_{\rm cm}^{(0)}$. The difference $\bar{V}_{\rm cm}^{0} - \bar{V}_{\rm cm}$ then yields the vertical air velocity.

3.2. Retrieval of N_0 and R

[17] For the light rain examined here, R is generally less than a few millimeters per hour, and we can neglect attenuation due to the rain and ice particles at 3.1-cm wavelength [*Battan*, 1973]. For simplicity, we also ignore the melting band attenuation at the centimeter wavelength which is about 1 dB for two way [*Bellon et al.*, 1997]. This assumption will not affect the estimates of D_0 and w but will introduce a systematic error in certain retrieved parameters such as rainfall rate and rain attenuation. Neglecting melting band attenuation at centimeter wavelength will result to an underestimation of N_0 by about 20–25%, consequently, underestimating the rainfall rate and the rain attenuation and overestimating the water vapor attenuation by about 20–25%. From equations (2) and (11), we then have

$$Z_{\rm cm}/N_0 = Z_{\rm cm}^{(t)}/N_0 = c_Z \int_{D_{\min}}^{D_{\max}} D^{\mu} \exp\left(-\frac{(3.67+\mu)D}{D_0}\right)\sigma_{\rm BACK,cm}(D)\mathrm{d}D. \quad (14)$$

The right hand side of this equation is a function of μ and D_0 only. Once D_0 is known, this equation can be used to calculate N_0 and hence the rainfall rate.

3.3. Retrieval of Melting Band and Water Vapor Attenuation at the Millimeter Wavelength

[18] Let r_0 be the range from the radar to the range bin just below the melting band. The reflectivity at r_0 is given by

$$\xi_{\rm mm}(r_0) = \xi_{\rm mm}^{(t)}(r_0) - \alpha_{\rm mm}(0, r_0). \quad (15)$$

The term $\alpha_{\rm mm}(0, r_0)$ represents the attenuation by the medium between the radar and range r_0. It is due mostly to any supercooled water above the melting band and the particles in the melting band. We identify it *nominally* as the melting band attenuation, $\alpha_{\rm mm,MB}$. Then

$$\alpha_{\rm mm,MB} = \alpha_{\rm mm}(0, r_0) = \xi_{\rm mm}^{(t)}(r_0) - \xi_{\rm mm}(r_0). \quad (16)$$

The measured reflectivity at r_0 provides an estimate of $\xi_{\rm mm}(r_0)$. The true reflectivity $\xi_{\rm mm}^{(t)}$ can be calculated using the retrieved RSD and backscattering cross section. However, we calculate $\xi_{\rm mm}^{(t)}$ using only the parameters $\Delta\bar{V}$, $Z_{\rm cm}$, and $\Delta\xi^{(t)}$, the difference of the reflectivity at the two wavelengths. $\Delta\xi^{(t)}$(dBZ) is a function of μ and D_0 or equivalent of μ and $\Delta\bar{V}$,

$$\Delta\xi^{(t)} \equiv \left(\xi_{\rm cm}^{(t)} - \xi_{\rm mm}^{(t)}\right) = f_\xi(\mu, \Delta\bar{V}). \quad (17)$$

The magnitude of f_ξ is a measure of the strength of Mie scattering at the shorter wavelength. Figure 1b shows that at small D_0, f_ξ is small because small drops predominate, and they scatter in the Rayleigh regime at both the wavelengths. As D_0 increases, f_ξ increases as the relative concentration of bigger drops, which scatter in the Mie regime at the shorter wavelength, increases. Combining equations (16) and (17), we get the nominal melting band attenuation,

$$\alpha_{\rm mm,MB} = [\xi_{\rm cm}(r_0) - \xi_{\rm mm}(r_0)] - f_\xi(\mu, \Delta\bar{V}(r_0)) \cong \left[\xi_{\rm cm}^{(\rm m)}(r_0) - \xi_{\rm mm}^{(\rm m)}(r_0)\right] - f_\xi(\mu, \Delta\bar{V}(r_0)), \quad (18)$$

which is the difference of the measured reflectivities at the two wavelengths adjusted for non-Rayleigh scattering. If the scattering were Rayleigh at both wavelengths, f_ξ would vanish and the attenuation would simply be the difference of the measured reflectivities at the longer (nonattenuating) and the shorter (attenuating) wavelengths.

[19] An equation similar to equation (18) for $r > r_0$ is

$$\alpha_{\rm mm}(0, r) \cong \left[\xi_{\rm cm}^{(\rm m)}(r) - \xi_{\rm mm}^{(\rm m)}(r)\right] - f_\xi(\mu, \Delta\bar{V}(r)). \quad (19)$$

The total attenuation between the radar and range r on the left-hand side can be decomposed into the total attenuation between the radar and r_0 ($\alpha_{\rm mm,MB}$) and the attenuation between r_0 and r due to gases and precipitation,

$$\alpha_{\rm mm}(0, r) = \alpha_{\rm mm,MB} + \alpha_{\rm mm}(r_0, r) = \alpha_{\rm mm,MB} + \alpha_{\rm mm}^{(\rm gas)}(r_0, r) + \alpha_{\rm mm}^{(\rm ppt)}(r_0, r). \quad (20)$$

Combining equations (19) and (20), we get the integrated water vapor attenuation,

$$\alpha_{\rm mm}^{(\rm gas)}(r_0, r) = \left\{\left[\xi_{\rm cm}^{(\rm m)}(r) - \xi_{\rm mm}^{(\rm m)}(r)\right] - f_\xi(\mu, \Delta\bar{V}(r))\right\} - \alpha_{\rm mm,MB} - \alpha_{\rm mm}^{(\rm ppt)}(r_0, r). \quad (21)$$

All the terms on the right-hand side of equation (21), except the last term, are known from measurements or have been estimated above. Thus in order to estimate the water vapor attenuation, we need to find the integrated precipitation

attenuation. Again, this quantity can be calculated without making explicit use of N_0, D_0, and the extinction cross sections. Noticing that $k_{mm} / Z_{cm}^{(t)}$ is independent of N_0 and is a function only of μ and D_0, we can write

$$k_{mm}^{(ppt)} / Z_{cm}^{(t)} = f_{k/Z}(\mu, \Delta\bar{V}). \quad (22)$$

Figure 1c shows that, for a given μ, $k_{mm}^{(ppt)}/Z_{cm}^{(t)}$ increases as $\Delta\bar{V}$ decreases, and for a given $\Delta\bar{V}$ less than its maximum value, $k_{mm}^{(ppt)}/Z_{cm}^{(t)}$ increases as μ decreases. Using the curves in Figure 1c, we can calculate $k_{mm}^{(ppt)}$ using Z_{cm}, μ, and $\Delta\bar{V}$. The integrated precipitation attenuation can be evaluated numerically using

$$\alpha_{mm}^{(ppt)}(r_0, r) = c_k \int_{r_0}^{r} Z_{cm}(r') f_{\kappa/Z}(\mu, \Delta\bar{V}(r'))dr'. \quad (23)$$

4. Data Description

[20] The radar data used in this paper were collected from a widespread light stratiform rain with a melting band on 11 July 2002 by EDOP and CRS during the CRYSTAL-FACE field campaign. Both radars were installed on NASA's ER-2 aircraft. The aircraft flies at an altitude of 20 km with a ground speed of approximately 210 m s^{-1}. The radar characteristics are summarized in Table 1, and detailed descriptions of the radars and data acquisition procedures may be found in the works of *Heymsfield et al.* [1996] and *Li et al.* [2004]. The beam widths of the radars gave ground footprints of approximately 1.0 × 1.0 km for EDOP and 0.28 (along track) and 0.21 (cross track) km for CRS. The signal integration time for the radars is 0.5 s, and the aircraft travel approximately 100 m. The ground footprint of EDOP is 1 km; returns from 10 beams of the radar are averaged since these beams illuminate essentially the same scatterers. For similar reasons, two beams of CRS illuminate essentially the same scatterers. Since the footprint of EDOP is about 3.6 times that of CRS, eight beams from CRS are averaged along the flight direction to minimize the beam mismatch between the two radars.

[21] Sources of error in the observations include calibration errors, errors due to mismatch between the two radar beams and nonuniform distribution of scatterers, aircraft motion, and signal fluctuations. The calibration errors in both EDOP and CRS are less than 1 dBZ [*Li et al.*, 2004]. In our case, there is a substantial mismatch between the two radar beams. We have attempted to minimize the mismatch along the flight direction by beam averaging.

[22] Using the methods from *Doviak and Zrnic* [1993], we have estimated the errors due to signal fluctuations on Doppler velocities at both wavelengths. These errors, 0.042 m s^{-1} for EDOP and 0.025 m s^{-1} for CRS, are much smaller than errors due to the aircraft motion, which is about 0.3 m s^{-1} estimated from the Doppler velocity over the clear ocean surface. The error due to the aircraft motion affects the individual Doppler velocities; however, it does not affect the difference of Doppler velocity at the two wavelengths. The error in ΔV due to the signal fluctuation is about 0.05 m s^{-1}. We also conducted error analysis of retrieved parameters because of signal fluctuations. The results can be summarized as follows: (1) For $\mu = 0$, the error in D_0 is generally less than about 0.03 mm for $\Delta\bar{V}^{(m)} < 3$ m s^{-1}. The error increases rapidly for $\Delta\bar{V}^{(m)} > 3$ m s^{-1} and has a singularity at the maximum $\Delta\bar{V}^{(m)}$. Also for other things being equal, the error increases with increasing μ. (2) The relative error in R is less than 13% with calibration error of 1 dBZ in reflectivity and 0.1 m s^{-1} errors in $\Delta\bar{V}$; (3) the error in melting band attenuation at millimeter wavelength is less than 2 dB; (4) For $0.5 < \Delta\bar{V} < 3$ m s^{-1}, the error in integrated gas attenuation is about 1.5 dB for $Z_{cm} = 20$ dBZ and 2.5 dB for $Z_{cm} = 30$ dBZ. The error increases rapidly for $\Delta\bar{V} < 1$ m s^{-1} or > 3 m s^{-1}.

Table 1. Characteristics of the Radars

	EDOP	CRS
Wavelength (cm)	3.115	0.32
Peak Power (kW)	7.6	1.7
Beam Width (°)	2.9 (circular)	0.6 (cross-track), 0.8 (along track)
Pulse Width (μs)	0.5	1.0
PRF (kHz)	4.444	4, 5 (dual PRF)
Antenna Gain (dB)	36.1 (nadir), 35.5 (forward)	46.4
Range Gate (m)	37.5	37.5

5. Results

[23] In this section, we present the retrieved parameters for the entire area for selected values of μ and their horizontally averaged vertical profiles. Figure 2 shows the flight path, and Figure 3 shows a nearby sounding. Figure 4 shows observed reflectivities and Doppler velocities from both radars. The top of the melting band is at a height of about 4.3 km above ground. The pronounced decrease of reflectivity at the shorter wavelength below the melting band indicates severe attenuation in rain. A number of precipitation trails in the field of the longer wavelength reflectivity and Doppler velocity (Figures 4a and 4b) can be followed from the ice down into the rain region. The reflectivities increase at the intersection of the trails with the melting band. Before presenting the results of the retrieved parameters, we discuss methods for constraining the values of the shape parameter μ.

5.1. Constraints on μ

[24] We use one value of μ for the entire field. It is conceivable that μ varies systematically with the height with larger values occurring near the ground. Unfortunately, we did not have enough independent measurements to retrieve all three parameters of the RSD. The value of μ can be constrained by the measured Doppler velocities coupled with the calculations presented in section 3 and the retrieved data coupled with the known properties of widespread stratiform precipitation. We discuss the former constraint below while the latter will be discussed in section 5.2.

[25] Figure 5 shows a scatterplot of observed mean Doppler velocity at the longer wavelength $\bar{V}_{cm}^{(m)}$, corrected for air density, against the observed differential Doppler velocity $\Delta\bar{V}^{(m)}$. The figure also includes the theoretical relationship between $\bar{V}_{cm}^{0}$ and $\Delta\bar{V}$ for $\mu = -2, -1, 0, 1, 2, 4, 6$. The curve for each μ has a maximum $\Delta\bar{V}$. Since $\Delta\bar{V}$ is

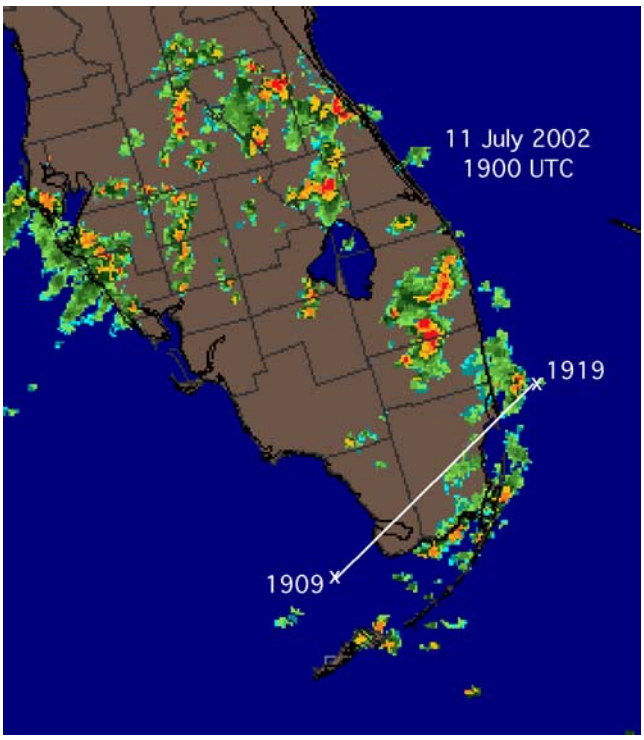

Figure 2. Flight track for 1903–1919 UTC on 11 July 2002. The background is a composite radar reflectivity image from the National Weather Service WSR-88D radars. The stratiform cloud studied is at the end of the flight line on the east coast of Florida.

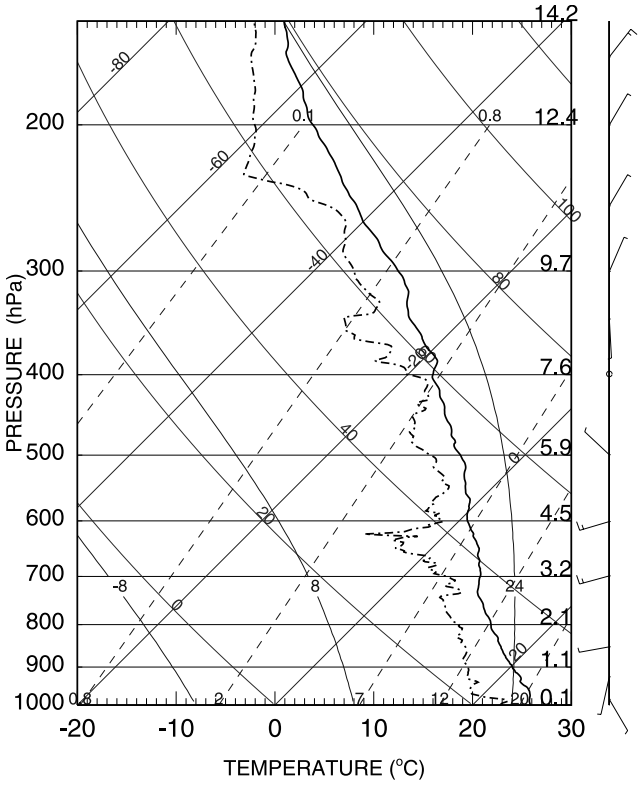

Figure 3. Miami sounding at 1936 UTC on 11 July 2002.

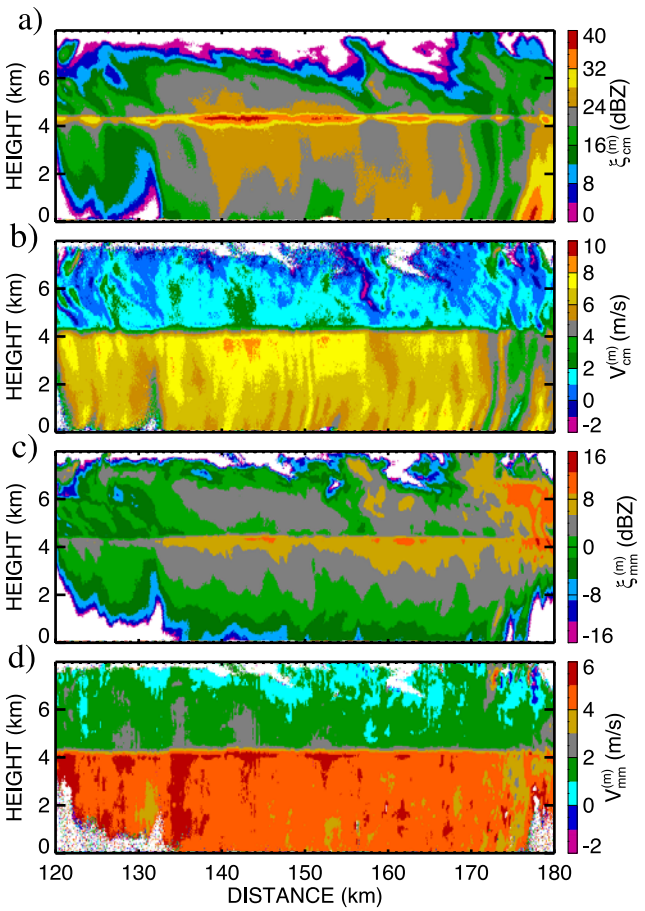

Figure 4. (a) Reflectivity measured at 3.1-cm wavelength, $\xi_{cm}^{(m)}$; (b) Doppler velocity at 3.1-cm wavelength, $\bar{V}_{cm}^{(m)}$; (c) Reflectivity at 3.2-mm wavelength, $\xi_{cm}^{(m)}$; and (d) Doppler velocity at 3.2 mm wavelength, $\bar{V}_{cm}^{(m)}$ during 1909–1919 UTC on 11 July 2002.

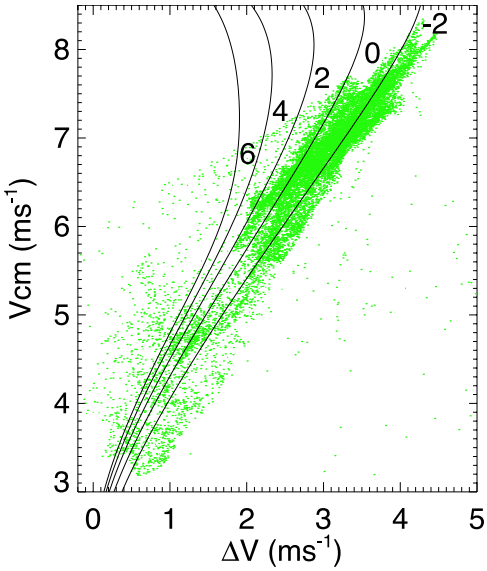

Figure 5. Scatterplot of the observed Doppler velocity at 3.1-cm wavelength versus differential Doppler velocity at the two wavelengths overlaid by the theoretical curves for $\mu = -2$, 0, 2, 4, and 6.

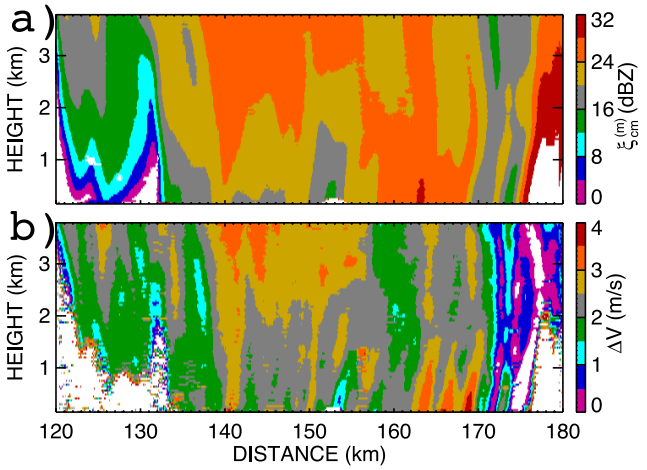

Figure 6. (a) Measured reflectivity at centimeter wavelength ($\xi_{cm}^{(m)}$), (b) difference of the Doppler velocity measured at two wavelengths ($\Delta\bar{V}$).

unaffected by vertical air velocity and attenuation, values of $\Delta\bar{V}$ greater than the maximum for a given μ are impossible for a RSD with that μ. Thus a differential Doppler velocity greater than about 2.9 m s^{-1} is impossible with $\mu \geq 2$. Since a substantial fraction of the observations lie to the right of $\Delta\bar{V}$ = 2.9 m s^{-1}, $\mu \geq 2$ can not explain a majority of the observations. We also note that a very small fraction of the observations, lying in the upper right corner of the figure and having $\Delta\bar{V} > 3.6$ m s^{-1}, require a RSD with a negative μ.

[26] Given a value of μ, the vertical air velocity may be inferred with the help of Figure 5. A point on the theoretical curve for a given μ gives the $\bar{V}_{cm}$ that would be observed in the absence of vertical air motion. A vertical displacement of the points below (above) the theoretical curve implies an updraft (downdraft) equal to the magnitude of the displacement. We see that μ = 2 would yield mostly updrafts and often with magnitudes exceeding 1 m s^{-1}. A value of μ = 0 corresponds to more updrafts, often with magnitudes generally less than about 0.5 m s^{-1}. For $\mu \cong -1$, there are roughly equal frequencies of updrafts and downdrafts with only a small fraction of the points unexplained.

[27] In view of the above, only $\mu \leq 2$ is compatible with the observations. In the following, we will therefore present the results for $\mu = -2$, 0, 2 in order to examine their sensitivity to μ. A further refinement of the possible value of μ will be made later on the basis of the retrieval presented.

5.2. Retrieved D_0 and w

[28] The longer wavelength reflectivity and the differential Doppler velocity are included in Figure 6 for ease of comparison. Figures 7 and 8 are the retrieved D_0 and w fields for $\mu = -2$, 0, 2. Horizontal distance is measured from the beginning of the flight line in Figure 2.

[29] For the same value of μ, the trails in the D_0 field bear a resemblance to the trails in the longer wavelength reflectivity and mean Doppler velocity fields. The white regions in the figure for μ = 0 represents regions of noisy signal. The additional white regions in the retrievals for $\mu = -2$, 2

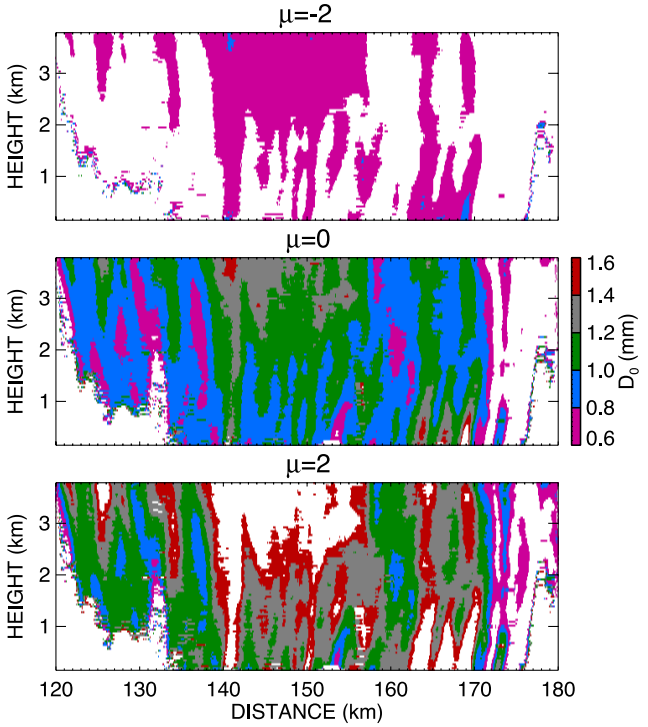

Figure 7. Retrieved D_0 from $\Delta\bar{V}$ for $\mu = -2$, 0, and 2. The white regions in the plots of $\mu = -2$ and 2 is where the data are incompatible with these values of μ. See text for detail.

represent regions in which the data are incompatible with these values of μ. The image of D_0 for $\mu = \pm 1$ (not shown) are similar to that for μ = 0 except that D_0 is about 0.2 mm larger for μ = 1 and 0.2 mm smaller for $\mu = -1$.

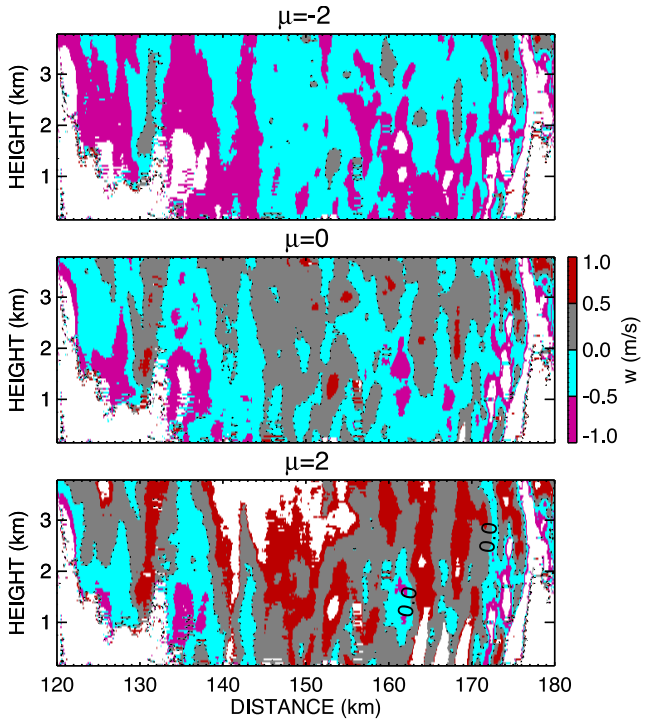

Figure 8. Retrieved w. The white regions in the plot of $\mu = -2$ and 2 are where the w retrieval is not possible with these values of μ. See text for detail.

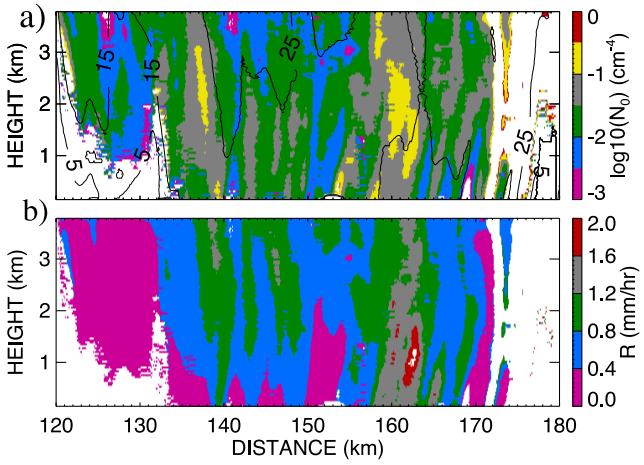

Figure 9. (a) Retrieved N_0; (b) Rainfall rate R calculated from the retrieved N_0 and D_0, for $\mu = 0$. Contour lines are the reflectivity measured at centimeter wavelength.

[30] The retrieved w field (Figure 8) for $\mu = 0$ also exhibits a trail structure somewhat similar to that of the $\xi_{cm}^{(m)}$ field, but it is not as organized as that of D_0 field. The error in w, 0.3 m s^{-1} considering aircraft turbulent motion, corresponds to about one interval of the w color scale. For $\mu = 0$, the magnitude of the vertical air motions is generally less than 0.5 m s^{-1}. Downdrafts greater than about 1 m s^{-1} occur at the near edge of the plotted reflectivity field, where the radar echo does not reach the ground, and in the lower levels in the region around 135 km. These regions have smaller D_0 values. A few small pockets of about 1 m s^{-1} upward air motion occur in the upper levels. Again, the figures show that for $\mu = -2$, 2, the retrieved w is unrealistic; there is a preponderance of updrafts for $\mu = 2$ and a preponderance of downdrafts for $\mu = -2$. The magnitudes of the vertical air velocities for $\mu = -2$, 2 often exceed 1 m s^{-1}. The retrieved values for $\mu = 0$ are consistent with observations of vertical air velocity in widespread stratiform rain. Indeed, a magnitude of the vertical air velocity of 0.5 m s^{-1} has often been used to classify precipitation into convective and stratiform types [*Houze*, 1993]. However, a slightly negative μ will result in a retrieved w fields that is similar to Houze's conceptual model, where there are more downdrafts than updrafts at low levels in the stratiform region, and with mean downward motion forming a region of mesoscale descent below the melting layer as will be shown later in Figure 14d.

5.3. Retrieved N_0 and R

[31] The retrieved N_0 and R fields shown in Figure 9 for $\mu = 0$ have trail structures similar to the reflectivity field. The retrievals for $\mu = -2$, 2 (not shown) are similar except that, when $\mu = 2(-2)$, N_0 is lower (higher) and R is higher (lower). A histogram of N_0 for $\mu = -1$, 0, 1 (Figure 10) shows that, for $\mu = -1$, 0, the N_0 values vary over more than two orders of magnitude and are generally less than the Marshall-Palmer value. *Waldvogel* [1974] reported observations of RSD in stratiform rain with a ground-based electromechanical raindrop spectrometer. His time series of N_0 (see, for example, his Figure 2) also show values of N_0 less than the Marshall-Palmer value and variations in N_0 of over two orders of magnitude. *Uijlenhoet et al.* [2003] reported disdrometer observations of RSD for a squall line. They found values of N_0 smaller than the M-P value in the transition and stratiform regions of the storm. In particular, in the stratiform portion of the rain, their N_0 values were generally less than 3×10^{-2} cm^{-4}, which is the mode value in our histogram plot of N_0 for $\mu = 0$.

[32] The general Z-R relation is important for space-borne precipitation measurements because of its simplicity, and also because reflectivity is the only parameter available on either TRMM PR or upcoming GPM DPR. The Doppler-based approach presented in this paper can estimate RSD directly, and it may provide a more accurate Z-R relation for light stratiform rain. We now compare the Z-R relation from the Doppler-based approach with some other Z-R relations in the previous studies. Figure 11 gives a scatterplot of $\xi_{cm}^{(m)}$ versus retrieved R for $\mu = 0$ with a best fit for $\mu = -1$, 0, 1. Three other Z-R relations for stratiform rain from Marshall-Palmer (M-P), Darwin, Australia [*Tokay and Short*, 1996] and that used by TRMM precipitation radar [*Iguchi et al.*, 2000] are also shown. There is a fair agreement between the slopes of the various Z-R relations. The best fit line for $\mu = 1$ is slightly above the other Z-R relations, and it has the best agreement with relation used by TRMM. The best fits for $\mu = -1$, 0 are between the other Z-R relations. As shown here, R derived from the Doppler-based Z-R relation is about 36% (for $\mu = 0$) and 64% (for $\mu = -1$) higher than that from the currently used TRMM relation (i.e., *Iguchi et al.*, 2000). This one example indicates that the additional velocity information can help understand the biases in the satellite- and ground-based R for light rain.

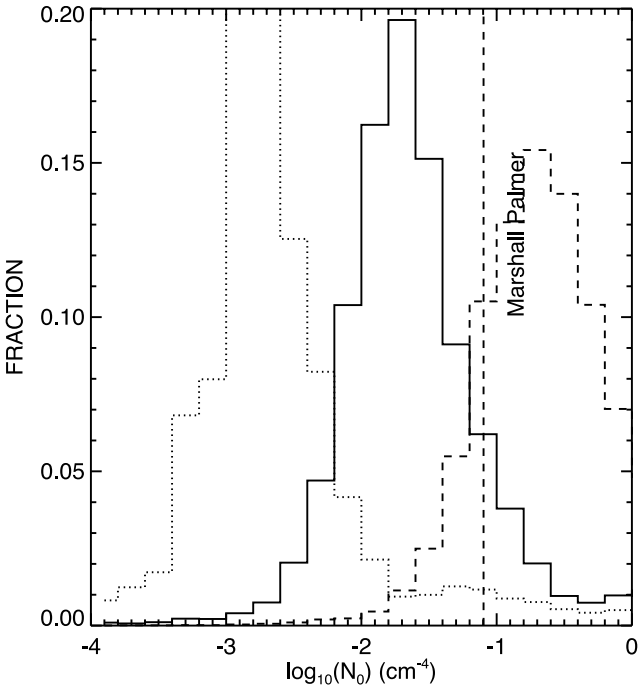

Figure 10. Histogram of retrieved N_0 values for $\mu = -1$ (dotted dash), 0 (solid), and 1 (dash). $\log_{10}(N_0) = -1.1$ ($N_0 = 0.08$ cm^{-4}) (vertical dashed line) is for Marshall Palmer distribution.

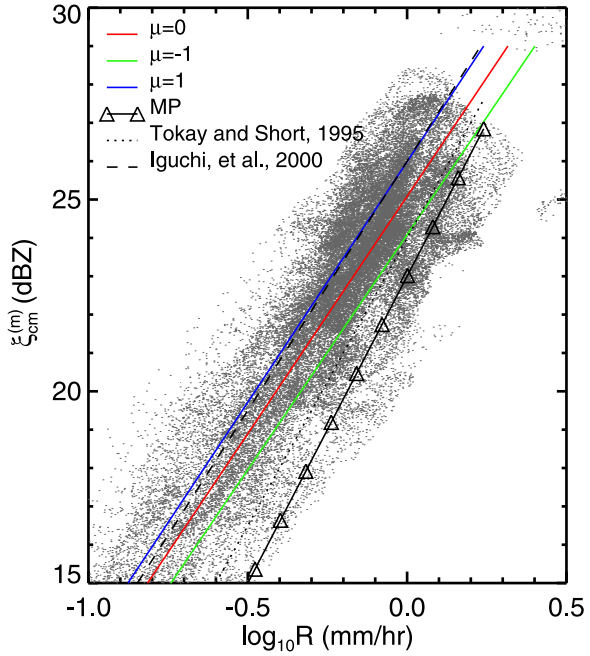

Figure 11. Scatterplot of $\xi_{cm}^{(m)}$ against retrieved R for $\mu = 0$. The colored lines are the best fit of $\xi_{cm}^{(m)}$ and R for $\mu = -1$ (green), 0 (red), and 1 (blue). Three other Z-R relations for stratiform rain are also shown (see text for detail).

5.4. Retrieved Melting Band and Water Vapor Attenuation

[33] Figure 12 shows the retrieved nominal two-way melting band attenuation, $\alpha_{mm,MB}$ (strictly, the two-way millimeter-wavelength attenuation by precipitation particles and water vapor from the radar to just below the melting band) and $\xi_{cm}^{(m)}$, the maximum centimeter-wavelength reflectivity in the melting band, as functions of the horizontal distance. The peak value of $\alpha_{mm,MB}$ is about 10 dB for $\mu = 0$ while its average value is about 5 dB; of this, a maximum of about 1.5 dB can be attributed to attenuation by water vapor and clouds above the melting band. There is a positive correlation between $\alpha_{mm,MB}$ and $\xi_{cm,MB}$. The estimated error in the melting band attenuation due to signal fluctuation is less than 1–2 dB. The variation of meting band attenuation with μ is about 1 dB for $\mu = \pm 1$.

[34] Figure 13 shows the retrieved two-way integrated water vapor attenuation for horizontal ranges between 135 and 170 km (the millimeter-wave signal is weak or noisy in the other regions) for $\mu = -2$, 0, 2. Consider first the retrieval for $\mu = 0$. We notice that the water vapor attenuation is highly variable. The variability is vaguely suggestive of a trail structure in the integrated attenuation. The estimated error in the gaseous attenuation, integrated from just below the melting band to near the ground due to signal fluctuation, is approximately 2 dB for $\sigma(\Delta\bar{V}) = 0.05$ m s^{-1} and $\Delta\bar{V}$ between 1 and 3 m s^{-1}; this error increases rapidly as (1) $\Delta\bar{V}$ exceeds 3 m s^{-1} or decreases to less than 1 m s^{-1} and (2) $Z_{cm}^{(m)}$ increases for $\Delta\bar{V}$ less than about 1.5 m s^{-1}. For $\mu = -2$, the retrieved attenuations are smaller and produce negative values in some regions. These regions are incompatible with an RSD having $\mu = -2$. For $\mu = 2$, the retrieved attenuations are larger, and there are

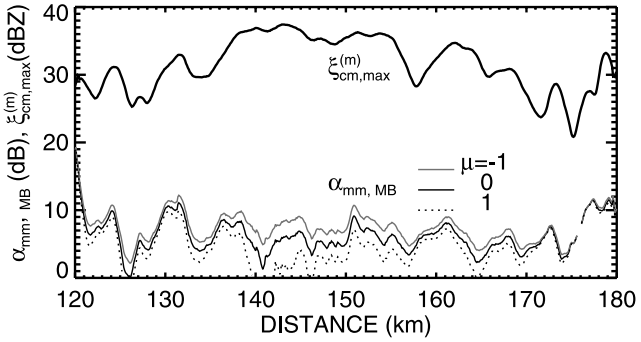

Figure 12. Two-way integrated melting band attenuation at millimeter wavelength for $\mu = -1$, 0, 1 and maximum reflectivity in the melting band ($\xi_{cm}^{(m)}$, thick solid line) along the flight line.

large regions where retrievals are impossible because D_0 cannot be retrieved. Thus $\mu \geq 2$ is also incompatible with the observations.

5.5. Horizontally Averaged Results

[35] Horizontally averaged profiles of certain observed and retrieved quantities for the region between 135 and 155 km, containing about 200 individual profiles, are presented in Figure 14 for $\mu = -2$, -1, 0, 1, 2. These profiles were obtained by averaging the individual retrieved profiles rather than by performing retrieval on the averaged profiles of the observed Doppler velocity and reflec-

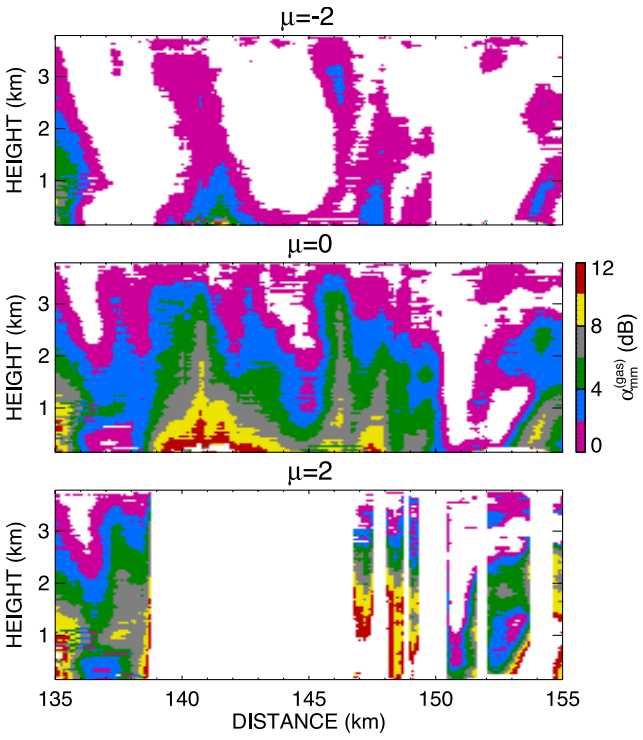

Figure 13. The retrieved two-way integrated water vapor attenuation at millimeter wavelength, $\alpha_{mm}^{(gas)}$ for $\mu = -2$, 0, and 2. Note that the integration starts from an 3.8-km height, right below the melting layer. So if the D_0 can not be retrieved at the 3.8-km height, $\alpha_{mm}^{(gas)}$ at the rest of range gate can not be retrieved as indicated by the white space in the figure.

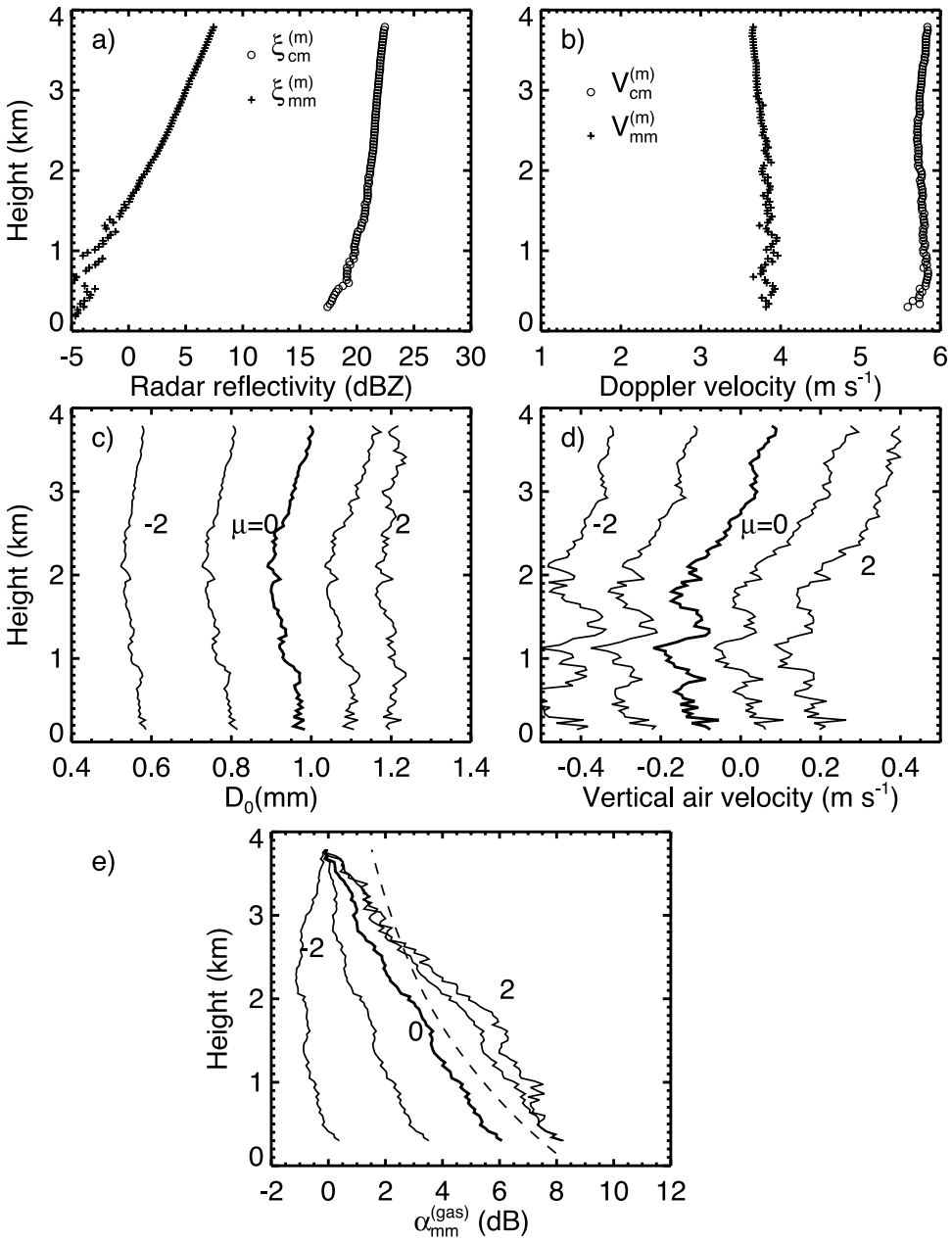

Figure 14. Horizontally averaged profiles are as follows: (a) Observed reflectivity and (b) Doppler velocity at centimeter and millimeter wavelength; (c) Retrieved D_0; (d) vertical air velocity, (e) two-way integrated water vapor attenuation, and (f) two-way integrated attenuation by precipitation for $\mu = -2$, -1, 0, 1, and 2, respectively. Dashed line in Figure 4e is the water vapor attenuation calculated from the sounding for a saturated atmosphere.

tivities. The averaging should reduce the random errors considerably since the individual profiles are independent.

[36] Figure 14a shows the average observed reflectivities for the two wavelengths. The strong attenuation suffered by the millimeter wavelength is evident. The downward decrease of the reflectivity at the centimeter wavelength is likely due to evaporation. The total decrease of reflectivity from the top to the bottom of the layer is about 5 dB. Figure 14b shows the averaged mean Doppler velocities. Figure 14c shows that the retrieved median volume diameter D_0 is very sensitive to the value of μ. Smaller values of μ yield smaller values of D_0. It shows that variation of D_0 is less than 0.2 mm or less than 20 % for $|\mu| \leq 1$. Figure 14d shows the vertical air velocity. The estimated error in the retrieved vertical air velocity, for a range bin, is about 0.3 m s^{-1}. The averaging of about 200 profiles should reduce the error by a factor of 14. Such reduction in the error is evident in the averaged profile, which shows only small range bin to range bin fluctuations. A change in μ displaces the curves horizontally. With $\mu = 2$ and -2, updrafts and downdrafts, respectively, prevail over the entire depth. For $\mu = -1$, 0, there are downdrafts present in the lower layers and updrafts above about 3-km height. This pattern of vertical velocity profile is typical of widespread stratiform rain found

in other studies [e.g., *Zipser*, 1977; *Houze*, 1993, chapter 9; *Srivastava et al.*, 1986]. The profile for $\mu = 0$ also shows a satisfactory decrease in the vertical air velocity to zero near the ground, whereas with $\mu = -2$ and $\mu = 2$, we get $w = -0.4$ and 0.2 m s^{-1}, respectively, near the ground. The variation of w for $|\mu| \leq 1$ is less than 0.2 m s^{-1}.

[37] Figure 14e shows the averaged retrieved profiles of integrated water vapor. As discussed before, the estimated error in individual profiles are about 2–4 dB. Thus the individual profiles are not very useful considering that the integrated gas attenuation for saturated atmosphere (dash line in Figure 14e), calculated from sounding in Figure 3 using the equation in the work of *Ulaby et al.* [1982], is about 8 dB. The averaging of 200 independent profiles reduces the error from 2–4 to about 0.15–0.3 dB. For $\mu = -2$, the profile shows negative values of the integrated attenuation over almost the entire depth. For $\mu = 1, 2$, the profiles show unphysical supersaturation. This enables us to constrain the value of μ to the interval of $(-1, 1)$. The great sensitivity of the retrieved water vapor attenuation to μ is both an advantage and a disadvantage. It means that useful water vapor profiles cannot be retrieved unless μ is known with great accuracy. Conversely, however, if water vapor distribution is known even approximately, the value of μ can be constrained fairly tightly. Thus the requirements of the impossibility of negative water vapor attenuation and supersaturation enable us to constrain the value of μ to the interval of $(-1, 1)$.

6. Summary and Discussion

[38] We have conducted an evaluation of the potential of nadir-looking dual-wavelength Doppler radar (EDOP −10 GHz and CRS−94 GHz) for retrieving the properties of light stratiform rain. Except for very large raindrops, the scattering at 10 GHz is in the Rayleigh regime while at 94 GHz it is in the Mie regime except for the very small raindrops. The signal at 10 GHz is subject to little or no attenuation in light rain while the signal at 94 GHz is subject to significant attenuation by rain and water vapor. Consequently, the mean Doppler velocity and reflectivity measured at the two frequencies are quite different. These differences have been exploited to retrieve Gamma RSD parameters, vertical air velocity, and attenuation by rain, melting band and water vapor. Horizontally averaged profiles have been presented. For these retrievals, we had to assume one value of the RSD shape parameter μ for the entire rain field.

[39] On the basis of the observed difference of the Doppler velocity at the two frequencies, the retrieved vertical air velocity, and the retrieved water vapor attenuation, we have shown that, if one value of μ is selected to apply to the whole rain field, then it is mostly likely to be in the interval of $(-1, 0)$. Many investigators have reported larger values of the parameter μ. For example, *Kozu and Nakamura* [1991], *Wilson et al.* [1997], *Tokay and Short* [1996], and *Bringi et al.* [2003] estimated that mean value of μ ranges from 2–6. These investigators have generally measured the RSD near the ground by disdrometer except Wilson et al. who used the differential Doppler velocity at two polarizations to estimate μ. The disdrometer is limited in its ability to measure small drops. Also, many of these observations relate to intense convective rains rather than light stratiform rain. *Maki et al.* [2001] reported extensive measurements of RSD in rains from squall lines in Darwin, Australia. They classified the rains into convective line, stratiform, and reflectivity trough. For the stratiform region they found the parameter μ to lie between −0.7 and 3.1 with a modal value of 1.3. Thus our value of μ is consistent with the results of Maki et al. *Tokay and Short* [1996] found that, for very light ($R < 1$ mm/hr) and light ($1 \leq R \leq 5$), $\mu = 1.7$ and 2.3. *Ulbrich and Atlas* [1998] found μ is sharply peaked at a modal value of $\mu = 0$ with a mean value of 1.67, with the central 80% of data occurring in range of $-2 < \mu < 5$.

[40] Lacking independent in situ or ground-based measurements, we have argued in favor of the validity of our retrievals on the basis of physical plausibility and consistency of our results and their agreement with properties of stratiform rain reported in the literatures. For $\mu = 0$, the retrieved parameters such as D_0 and the vertical air velocity have trail structures similar to those in observed reflectivity and mean Doppler velocity at the longer wavelength. The numerical values and scatter of the retrieved N_0 are similar to those found by others in ground-based studies of stratiform rain RSD. The retrieved melting band attenuation at the shorter wavelength has shown strong positive correlation with maximum reflectivity in the melting band at the longer wavelength. The profiles of the retrieved integrated water vapor attenuation have been found to be generally increasing with distance downward as would be expected. For $\mu = -1, 0$, the profile generally implied a subsaturated atmosphere as is physically plausible for extensive stratiform rain. The magnitudes and vertical variation of the vertical velocity are remarkably similar to what has been reported in the literature for area-averaged vertical velocity in extensive stratiform rains.

[41] The retrieved water vapor attenuation is very sensitive to the value of μ. This has two implications. First, to retrieve useful profiles of water vapor in rain, we need accurate value of μ and we need to consider its spatial variability. Secondly, even a poor knowledge of the water vapor distribution can help to constrain μ within a narrow interval of values. Thus from the physical requirement that water vapor attenuation at the millimeter wavelength must be positive and less than that for a saturated atmosphere, we were able to conclude that, if a single value of μ is applied to the entire rain field, it must be in the interval of $(-1, 0)$.

[42] The results presented in this paper have been based on certain assumptions. The most restrictive one is probably the assumption of a constant value of μ over the entire rain field. An assumption about the RSD parameters became necessary because with the available radar measurements, we could retrieve only two out of three RSD parameters. The assumption of a constant μ was adopted because it is the simplest and most direct assumption from the point of view of the retrieval of the RSD. Our results are also subject to errors because of mismatch between the two radar beams. We have attempted to minimize the effects of the mismatch along the flight path by averaging observations for an appropriate number of beams for each radar. This adjustment requires some degree of horizontal homogeneity of the reflectivity and Doppler velocity. However, the effects of beam mismatch in the cross-flight direction cannot be minimized. In future measurements, radar with matched beams should be employed.

[43] The potential ability to retrieve the parameters of the RSD, the vertical air velocity, and the water vapor distribu-

tion as functions of the height offers the possibility of direct calculation of profiles of evaporation and therefore latent cooling in the atmosphere using microphysical principles.

[44] In future studies, we will explore the possibility of using other radar parameters to retrieve μ. *Meneghini et al.* [2005] have reported on a feasibility study of using a triple wavelength system for determining all three parameters of the gamma function RSD and the water vapor distribution.

[45] The results presented have implications for the measurement of light rain with current and future spaceborne radars. The TRMM and future GPM radars estimate light rain with lower precision due to a variety of factors including the unknown RSD. These size distribution parameters are very difficult to obtain with ground-based radars or surface measurements. The approach developed here provides an independent method for estimating the RSD for light rain. The mean properties derived in this paper for the Gamma RSD in light rain utilize Doppler velocity. The example presented indicates that there can be significant underestimates for light rain retrieval algorithms for the TRMM PR. In addition to the current TRMM radar, the CloudSat W-band radar recently launched routinely samples light rain, but the R accuracy is yet to be determined. The results of this paper have focused on flight lines from 1 day during the CRYSTAL-FACE experiment; in future studies, we will explore how these results vary on other days and field experiments and also compare with in situ measurements.

[46] **Acknowledgments.** We thank Mr. Ed Zenker, Dr. Steve Bidwell, and Dr. Paul Racette for their engineering support of the radars. We also thank Dr. Meneghini for his helpful comments and suggestions. This work is supported by Dr. R. Kakar of NASA Headquarters under NASA's Precipitation Measurement Mission. The data were collected during the CRYSTAL-FACE campaign that was funded by the NASA Radiation Science Program. The work of Ramesh Srivastava is supported by NSF grant ATM 0314049.

References

Andsager, K., K. V. Beard, and N. F. Laird (1999), Laboratory measurements of axis ratios for large raindrops, *J. Atmos. Sci.*, *56*, 2673–2683.

Atlas, D. (1964), Advances in radar meteorology, *Adv. Geophys.*, *10*, 317–478.

Atlas, D., and T. J. Majetka (1985), Airborne Doppler radar velocity measurements of precipitation seen in ocean surface reflection, *J. Geophys. Res.*, *90*(D3), 5820–5828.

Atlas, D., R. C. Srivastava, and R. S. Sekhon (1973), Doppler radar characteristics of precipitation at vertical incidence, *Rev. Geophys. Space Phys.*, *11*, 1–35.

Battan, L. (1973), *Radar Observation of the Atmosphere*, p. 324, Univ. of Chicago Press, Chicago, Ill.

Bellon, A., I. Zawadzki, and F. Fabry (1997), Measurements of melting layer attenuation at x-band frequencies, *Radio Sci.*, *22*, 943–955.

Bringi, V. N., V. Chandrasekar, and J. Hubbert (2003), Raindrop size distribution in different climatic regimes from disdrometer and dual-polarized radar analysis, *J. Atmos. Sci.*, *60*, 354–365.

Doviak, R. J., and D. S. Zrnic (1993), *Doppler Radar and Weather Observations*, p. 562, Elsevier, New York.

Eccles, P. J., and E. A. Muller (1971), X-band attenuation and liquid water content estimation by a dual-wavelength radar, *J. Appl. Meteorol.*, *10*, 1252–1259.

Foote, G. B., and P. S. du Toit (1969), Terminal velocity of raindrops aloft, *J. Appl. Meteorol.*, *8*, 249–253.

Fujita, M. (1983), An algorithm for estimating rain rate by a dual-frequency radar, *Radio Sci.*, *18*, 697–708.

Haddad, Z. S., J. P. Meagher, and S. L. Durden (2006), Drop size ambiguities in the retrieval of precipitation profiles from dual-frequency radar measurements, *J. Atmos. Sci.*, *64*, 204–217.

Heymsfield, G. M., S. W. Bidwell, I. J. Caylor, S. Ameen, S. Nicholson, W. Boncyk, L. Miller, D. Vandemark, P. E. Racette, and L. R. Dodd (1996), The EDOP radar system on the high-altitude NASA ER-2 aircraft, *J. Atmos. Oceanic Technol.*, *13*, 795–809.

Houze, R. A. (1993), *Cloud Dynamics*, chapter 9, p. 570, Elsevier, New York.

Iguchi, T., T. Kozu, R. Meneghini, J. Awaka, and K. Okamoto (2000), Rain-profiling algorithm for the TRMM precipitation radar, *J. Appl. Meteorol.*, *39*, 2038–2052.

Kozu, T., and K. Nakamura (1991), Rainfall parameter estimation from dual-radar measurements combining reflectivity profile and path-integrated attenuation, *J. Atmos. Oceanic Technol.*, *8*, 259–271.

Kummerow, C., et al. (2000), The status of the tropical rainfall measuring mission (TRMM) after two years in orbit, *J. Appl. Meteorol.*, *39*, 1965–1982.

Li, L., G. M. Heymsfield, P. E. Racette, L. Tian, and E. Zenker (2004), A 94-GHz cloud radar system on a NASA high-altitude ER-2 aircraft, *J. Atmos. Oceanic Technol.*, *21*, 1378–1388.

Maki, M., T. D. Keenan, Y. Sasaki, and K. Nakamura (2001), Characteristics of the raindrop size distribution in tropical continental squall lines observed in Darwin, Australia, *J. Appl. Meteor.*, *40*, 1393–1412.

Marshall, J. S., and W. M. K. Palmer (1948), The distribution of raindrops with size, *J. Meteorol.*, *5*, 165–166.

Marzoug, M., and P. Amayenc (1994), A class of single- and dual-frequency algorithms for rain-rate profiling from a space-borne radar: Part 1. Principle and tests from numerical simulations, *J. Atmos. Oceanic Technol.*, *11*, 1480–1506.

Meneghini, R., T. Kozu, H. Kumagai, and W. C. Boncyk (1992), A study of rain estimation methods from space using dual-wavelength radar measurements at near-nadir incidence over ocean, *J. Atmos. Oceanic Technol.*, *9*, 364–382.

Meneghini, R., S. W. Bidwell, R. Rincon, G. M. Heymsfield, and L. Liao (2003), Differential-frequency Doppler weather radar: Theory and experiment, *Radio Sci.*, *38*(3), 8040, doi:10.1029/2002RS002656.

Meneghini, L. Liao, and L. Tian (2005), A feasibility study for simultaneous measurements of water vapor and precipitation parameters using a three-frequency radar, *J. Appl. Meteorol.*, *44*, 1511–1525.

Mishchenko, I. M., D. T. Larry, and A. A. Lacis (2003), *Scattering, Absorption and Emission of Light by Small Particles*, 462, Cambridge Univ. Press, New York.

Schumacher, C., and R. A. Houze Jr. (2003), Stratiform rain in the tropics as seen by the TRMM Precipitation Radar, *J. Clim.*, *16*, 1739–1756.

Srivastava, R. C., T. J. Matejka, and T. J. Lorello (1986), Doppler-radar study of the trailing anvil region associated with a squall line, *J. Atmos. Sci.*, *43*, 356–377.

Stephens, G. L., et al. (2002), The CloudSat Mission and the A-Train, *Bull. Amer. Meteor. Soc.*, *83*, 1771–1789.

Pruppacher, H. R., and R. L. Pitter (1971), A semi-empirical determination of the shape of cloud and raindrops, *J. Atmos. Sci.*, *28*, 86–94.

Tao, W.-K., S. Lang, W. S. Olson, R. Meneghini, S. Ynag, J. Simpson, C. Kummerow, E. Smith, and J. Halverson (2000), Retrieved vertical profiles of latent heat release using TRMM rainfall products for February 1998, *J. Appl. Meteorol.*, *6*, 957–982.

Tokay, A., and D. A. Short (1996), Evidence from tropical raindrop spectra of the origin of rain from stratiform versus convective clouds, *J. Appl. Meteorol.*, *35*, 355–371.

Uijlenhoet, R., M. Steiner, and J. A. Smith (2003), Variability of raindrop size distribution in a squall line and implications for radar rainfall estimate, *J. Hydrol.*, *4*, 43–61.

Ulaby, F. T., R. K. Moore, and A. K. Fung (1982), Microwave Remote Sensing: Active and Passive, vol. 1, p. 607, Addison-Wesley, Boston, Mass.

Ulbrich, C. W. (1983), Natural variations in the analytical form of the raindrop-size distribution, *J. Clim. Appl. Meteorol.*, *22*, 1764–1775.

Ulbrich, C. W. (1991), Algorithms for determination of rainfall integral parameters using reflectivity factor and mean Doppler fall speed at vertical incidence, *J. Atmos. Oceanic Technol.*, *9*, 120–128.

Ulbrich, C. W., and D. Atlas (1998), Rainfall microphysics and radar properties: Analysis methods for drop size spectra, *J. Appl. Meteorol.*, *37*, 912–923.

Waldvogel, A. (1974), The N_0 jump of raindrop spectra, *J. Atmos. Sci.*, *31*, 1067–1078.

Wilson, D. R., A. J. Illingworth, and T. M. Blackman (1997), Differential Doppler velocity: A radar parameter for characterizing hydrometeor size distributions, *J. Appl. Meteorol.*, *36*, 649–663.

Zipser, E. J. (1977), Mesoscale and convective-scale downdrafts as distinct components of squall-line circulation, *Mon. Wea. Rev.*, *105*, 1568–1589.

G. M. Heymsfield and L. Tian, NASA Goddard Space Flight Center, Greenbelt, MD 20771, USA. (tian@agnes.gsfc.nasa.gov)

L. Li, Goddard Earth Science and Technology Center, University of Maryland, Baltimore, MD, USA.

R. C. Srivastava, Department of the Geophysical Sciences, The University of Chicago, Chicago, IL, USA.